Confined impinging air jet on a heated cylinder at low Mach number

Éric Schall, Nicolas Chauchat, M. Mory

Confined impinging air jet on a heated cylinder at low Mach number

E. Schall[a], N. Chauchat[b] and M. Mory[c]

*[a] Corresponding author: UNIV PAU & PAYS ADOUR, LABORATOIRE DES SCIENCES DE L'INGÉNIEUR APPLIQUÉES À LA MÉCANIQUE ET AU GÉNIE ELECTRIQUE – IPRA, EA4581, 64000, PAU, FRANCE, eric.schall@univ-pau.fr (**CA**).*
[b] UNIV PAU & PAYS ADOUR, LABORATOIRE DES SCIENCES DE L'INGÉNIEUR APPLIQUÉES À LA MÉCANIQUE ET AU GÉNIE ELECTRIQUE – IPRA, EA4581, 64000, PAU, FRANCE, nicolas.chauchat@univ-pau.fr,
[c] UNIV PAU & PAYS ADOUR, IPRA, FR2952, 64000, PAU, FRANCE. mathieu.mory@univ-pau.fr.

Abstract:

Use of onboard electrical systems is vastly expanding in all aeronautical programs. This means that new cooling systems must increasingly be researched. More specifically, this paper focuses on the cooling of a small turbo engine, represented experimentally as a heating cylinder. This new cooling process designed at Pau University, France, provides quite an original experimental set-up. Given the confined nature of the motion fluid, only experimental measurements of medium physical values such as temperature and velocity can be made. In order to better understand and master such a cooling system, which seemingly could have many industrial applications, two different numerical simulations have been investigated. Because of the confined nature of the motion fluid (V=6.13 m/s, Mach=0.018) and the highly complex geometrics, no conclusion can be drawn about the fluid compressibility assumption. Therefore, the incompressible model study is carried out using ANSYS-FLUENT software whereas the compressible model study is conducted with ***elsA*** software. These two computer programs were chosen because of their capacity for double modelling in the hope that some of the major challenges facing the vast research community in the field of low Mach may be addressed. This study is carried out on two different scales. On the coarse scale there are significant similarities between the experimental results and some 2D simulations on the global convective wall heat flux (better than a 10% relative gap). On the smaller scale, code-to-code comparisons of both assumptions (via both codes) show different vortex structures inside the computational domain. Those vortices have a remarkable influence on the inner-wall heat flux's behaviour but their effect is moderate since their average values do not vary much. Though the velocity is relatively low inside the cavity, we will show that the fluid compressibility is of importance in such computations.

Keywords:

Air jet impingement, Laminar, compressible-incompressible modellings, Cylinder, Radial cooling system, Low Mach number, Green aircraft.

1. Introduction - Context

There are many reasons to encourage greater use of electrical power: pollution, fuel savings, environmental issues, etc. Increased electrical use appears to be unavoidable. Aerospace industries are not an exception to this rule. The aviation industry is committed to a veritable revolution in the field of energy systems onboard aircraft. Avionics is certain to witness the gradual replacement of hydraulic and pneumatic energy by electricity. The aeronautics sector has long favoured hydraulic energy, which is undoubtedly an efficient solution, but one that presents some major disadvantages. The aircraft's normal movements may cause leaks at components' connections. Moreover, circuits are interdependent and if one circuit fails, the other circuits may not be able to take over. Also, hydraulic fluid is corrosive and flammable. To overcome these problems, a new source of energy must be introduced. Already present in many low-power devices, electricity is currently being studied for devices requiring more power. Recent research work such as GREENAIR (FP7) and the

brand-new technological advances achieved on the A380 (Airbus 380) and the Boeing 787 clearly prove that the use of electricity is currently increasing.

As the use of electric-electronic devices increases, more and more efficient cooling systems are required. This study is part of a performance evaluation study of cooling systems for a turbo engine housing, represented experimentally by a small heating cylinder. In 2010 this research project was awarded the Aeronautics Industry Quality Certification label (France) by the three national aeronautical clusters. Funding has continued through 4 consecutive DGCIS-Research Fund grants (France). The original device to be studied can represent any small-sized engine and its potential could be immense in terms of industrial applications. Moreover, it is not restricted to the aeronautics sector. Indeed air jet impingement used for heat treatment is relevant to several engineering applications such as tempering of glass, cooling of turbine blades, drying of some industrial goods and cooling of electronic chips because of the high heat transfer coefficients which occur in the impingement region. Based on the pioneering work by Gardon and Akfirat [9] (along with others) the physics of jet impingement flows has been described in detail. A circular or slot impinging jet on a flat plate serves as a fundamental configuration for many others. Consequently, a multitude of studies have been devoted to these configurations [9-13]. Next, various shapes and nozzles used to generate jets impingement processing systems have been studied and reviewed by many authors. Similarly, applications of the impingement process using various target shapes are gaining popularity in industry. To perform studies of slot jets impinging on complex target shapes, authors often refer to available numerical and experimental findings on flat planes. In [14], for modelling selection and validation, results from various models are compared against test data for flat-plane jet impingement heat transfer, and a numerical turbulent model based on accuracy is selected to perform jet impingement flows over a cylindrical target surface. Though most reviews focus on the jet impingement cooling of flat surfaces, research into jet impingement on cylinders is expanding [15-20]. Impinging jets on cylinders can be tackled in two different ways: there are authors who consider slot jets to generate jet impingement [19-20] and those who consider circular jets [15-18]. Recently, in [17], the effect of nozzle shape on jet impingement heat transfer from a circular cylinder has been studied. Experimental and numerical investigations have been carried out to study the effect of different nozzle shapes - circular, square and rectangular. The air jet emerging from the nozzle and impinging on the circular cylinder is unconfined.

In the present study, three main points deserve to be mentioned in comparison to the existing works in the literature dealing with impingement jets. The first one is that the relative low flow magnitude allows us to consider the flow as laminar. Laminar impinging slot jets operating at low Reynolds numbers are often used for cooling of electronics components, especially when these involve either micro-scale fluid phenomena or micro-scale circuit components. The literature on jet impingement under the laminar assumption is very limited. In [21] different modes of unsteadiness which develop within confined, laminar impinging slot jets of millimetre-scale are considered. Experimental measurements and numerical predictions of different flow characteristics are investigated on a test surface with a constant surface heat flux boundary condition. H. Shariatmadar et al. [22] present a study of heat transfer from an isothermal target surface, which is impinged by an array of air-slot jets. This experimental and numerical study is focused on low Reynolds number ranging from 234 to 470. The variation in heat transfer in laminar wall jets with different initial velocity profiles is studied by Korovkin and Sokovishin [23]. They investigate the effect of the shape of the initial velocity profile on the development of the principle hydrodynamic and thermal parameters. The Reynolds number in their study is about 1400. According to the work by R. Gardon and J.C. Akfirat [24], in regimes of Reynolds number above 3000, impingement flows are essentially turbulent. As the Reynolds number is lower than 3000, the assumption of laminar flow is preferred to turbulent. Moreover, under the laminar assumption the wall heat flux can be easily calculated as follows: $\vec{q} = -\lambda \vec{\nabla} T$ where lambda is the thermal conductivity of the fluid and T its temperature. The second point is that we consider the compressibility effects in the numerical part of this work. To the best of our knowledge most numerical studies of jet impingement flows on

cylinders are devoid of any compressible effect [9-24]. Though the Reynolds number is relatively high and the flow is air, the assumption of incompressible flow is always made. However, the numerical study is performed for both compressible and incompressible fluid assumptions and the results are then compared. In the present work, the laminar flow field and heat transfer characteristics of radial slot jets impinging onto a heated cylindrical target surface are investigated numerically and experimentally. Air is used as the working fluid with constant properties taking into consideration uniform jet velocity exit impinging on a cylinder target surface of uniform temperature. Slot jet impingement has been studied frequently but relatively little has been published on cases where the cylinder is cooled circumferentially. Only N. Zuckerman et al. [13-14] carried out a numerical investigation on multiple slot jet impingement cooling of circular cylinders, with the nozzles placed circumferentially. They also investigate the effect of conduction in a finite thick cylinder with four impinging radial slot jets. In the present paper, compared to the work of N. Zuckerman et al., the geometry-size and the wall boundaries are different, the jet Reynolds number is one order of magnitude lower and the imposed wall heat flux is approximately seven times lower. An original experimental set-up of such a cooling system device was performed and numerical results compared to the experimental measurement can be considered as the third highlight of this paper.

This paper's main objective is to investigate this type of cooling process. To do this the authors used experience-numerical and numerical-numerical comparisons in two main directions: the first (experiment-numerical) deals with the convective heat flux transfer between the entrance and exit fluids. It should be noted that this comparison is global, i.e. on a large scale. Secondly, a more minute study was conducted through numerical-numerical comparisons to evaluate the effect of compressibility. This step is absolutely necessary since nothing can be deduced from the initial conditions (V=6.13 m/s, Mach=0.018). Logically, in the next step, the compressible and incompressible assumptions are tested and compared to each other. Because numerical simulations provide physical solutions at the scaled-particle level, finer comparisons were carried out, particularly on the wall heat flux's behaviour. Comparing experimental and numerical solutions is important, though objective and consistent analysis of results appears to be difficult to carry out even if the comparison is done properly. Indeed, in view of the significant number of parameters that have to be controlled for, there are many possible sources of errors and they are not easy to locate. In order to adjust the discussion frame (section 4), in the following two paragraphs we will attempt to globally identify errors in the experiment and the numerical simulation.

From the experimental point of view:

It is well worth pointing out that the confined aspect of the set-up reduces experimental measurement to intrusive measures (cf section 2). Though errors remain possible, no specific study will be conducted on this matter. In this study, measurements of temperatures and flow rate velocity, using respectively thermocouples and flow meters, are supposed to fix the boundary and initial conditions required for the numerical simulation. Finally, it should be noted that the temperature measurement given by thermocouples is always considered as “global” or “average”.

From the numerical point of view:

When compared to an experiment, numerical difficulties have to be taken into account differently. Assumptions must be made before computations, for at least one reason: no modelling associated with the numerical method is able to predict any fluid flow no matter what the value of the velocity magnitude or Mach number. Importantly, it must be mentioned that the latter applies to any numerical simulation in respect of a good estimate of accuracy, robustness and efficiency. The modelling through the partial difference equations (PDE) ensues from the conservative macroscopic balance of density, momentum and energy. While the experiment provides global physical values reduced to average temperature or medium velocity, numerical simulation can give any physical value (density, pressure, temperature and velocity) on the fluid particle's scale factor.

In this paper, the main fluid assumptions discussed are compressibility-oriented. Because the chosen velocity is relatively low (6.13m/s for a Mach number worth around 0.018), the decision to

consider or not the fluid's compressibility is definitely an important question. The steady or unsteady aspect is less easy to select because the mass flow rate is *a priori* a constant given by the experiment. Note that some instabilities can arise but they are hard to predict. As stated previously, the sub-objective is to make comparisons on the same simulation (i.e. with same initial boundary conditions) between those two different assumptions. To do this, the incompressible assumption will be computed by ANSYS-FLUENT while the compressible one will be computed by ***elsA***. Both these software programs are renowned in their field of expertise.

This study is organized into the following four sections. The original set-up is described in the next section, entitled Experimental design. Once the test case is defined, the numerical strategy is given in section 3 through a succinct presentation of the specific modelling used in the two programs. Results via both numerical-numerical and experience-numerical comparisons will be the discussion topic in the section that follows, entitled Commented results. The numerical-numerical comparison presented in this section is carried out with the results of the two models. Lastly, in the paper's conclusion and final section some of the main difficulties that a study of this kind tackles will be summarized. The nature of prospects in the field of numerical simulations highlights some of the main challenges for the future.

2. Experimental design

The experimental set-up achieves the cooling of the surface of a circular cylinder (radius R_i=5.4cm) by 4 plane jets, which perpendicularly impact the heated cylinder. As shown in Fig. 1, the four impacting jets are directed from the north, east, south and west, respectively. The heated air is extracted through four outlet slots (red arrows) whose directions run along the angle bisector between neighbouring inlet jets. The flow is confined to the annular domain with internal radius R_i and external radius R_f=7cm. The slot width is S_f=3.6mm. Numerical simulations were carried out assuming 2D flow, i.e. it varies in the direction Oz perpendicular to the cross-section shown in Fig. 1. The cylinder length is L=4.7cm in the experiment.

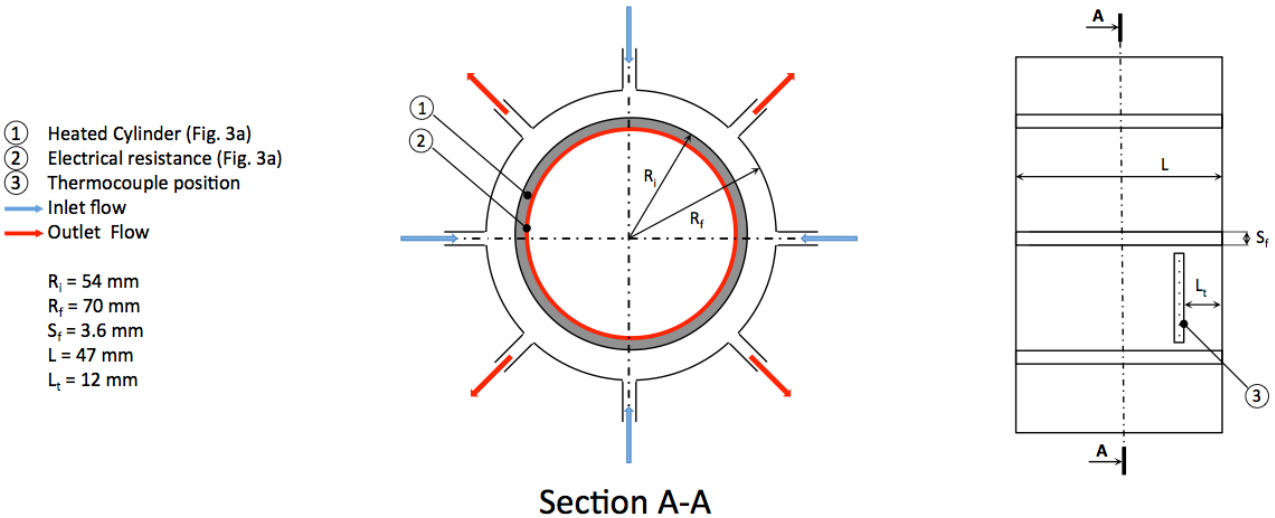

Fig. 1. View and cross-section of the cooling device with the heated cylinder of radius R_i.

Photograph in Fig. 2a shows the real experimental set-up. The blue arrows indicate the flow into four rectangular tubes leading to the cavity entrance slots. The casing that ensures the inlet distribution of the jets impacting the cylinder and collects the warm air outside the flow cavity is shown in Fig. 2b. The heated cylinder is inserted under the cone seen in Fig. 2b, which channels the exiting warm air into the vertical tube already seen in Fig. 2a. The red arrow indicates the direction of the outlet flow into a flexible tube, which is downstream, connected to a mass flow meter (Eldridge 9700MPNH), a fan and a valve. Note that the red arrow in Fig. 2a is the convergence point of the four red arrows (seen in Fig. 1), owing to a specific air-circulation design of the heating module (seen in Fig. 2b). The circular cylinder is heated using a 250W electrical resistance

previously inserted inside an adhesive polyamide mat glued over the inner surface of the cylinder (brown in Fig. 3a). The surface temperature on the cylinder is measured using thermocouples (type K). The wires of the thermocouples (green in Fig. 3a) traverse the mat and the cylinder (thickness 2mm) and the measuring extremities are bent after coming up to the cylinder surface. The entire surface of the cylinder is eventually wrapped in an adhesive film (resistant to high temperatures), which maintains the thermocouples in contact with the cylinder. Figure 3b gives an external view of the cylinder where the thermocouple measurement locations are shown.

2a   2b

Fig. 2. Photographs of the experimental set-up. 2a Blue arrows indicate the air entrance while the red arrow represents the exit. 2b Global view of the heating module including the four branches where the airflow enters.

The schematic below indicates that thermocouples 8, 9 and 12 are along the axis line of an impacting jet, whereas thermocouples 1, 10 and 11 are along the axis line of an outlet slot.

3a. 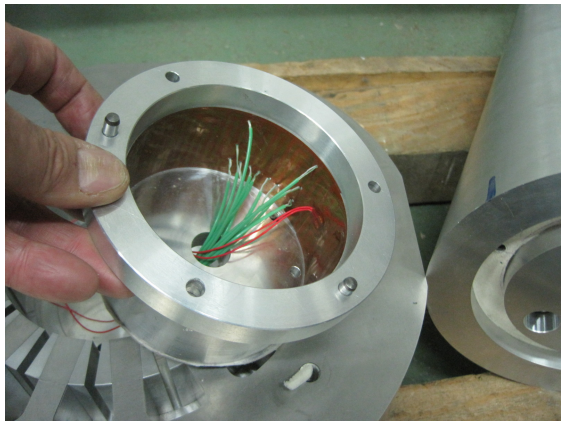 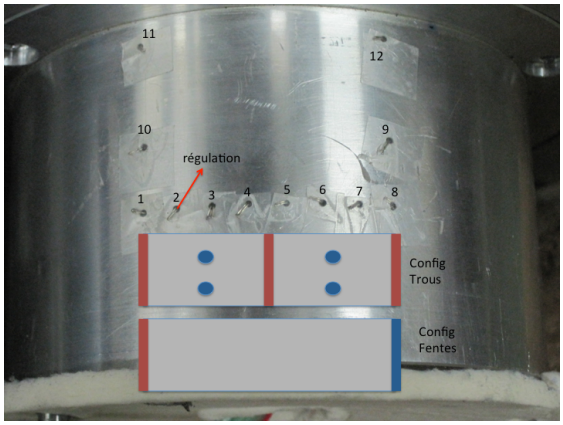

3b.

Fig. 3a. Inside view of the heated cylinder. Fig. 3b. Outside surface view of the heated cylinder showing the thermocouple positions. See Fig. 1 to locate the cylinder inside the cooling system.

The experimental conditions given by the mass flow rate and the electrical power Pelec result in the steady regime in the temperature level at the surface of the cylinder, which corresponds to the equilibrium between the furnished power and the cooling convective power. The present paper focuses on a flow condition with a relative low Reynolds number in a state of complex geometrics. Under such conditions, the electrical power delivered was reduced as compared to the maximum electrical power (420W) in order to maintain the surface temperature below 100°C (this is the

highest temperature the resistance polyamide mat can endure). The electrical power delivered was measured using a wattmeter. The thermal power $\Phi_{conv} = \dot{m} c_p (T_e - T_i)$ was also estimated from the temperature difference measured by two thermocouples (type K), one being placed inside one inlet tube (T_i) and the other (T_e) at the exit of an outlet slot from the cavity. An estimate of the average surface temperature T_{surf} was determined from the thermocouple measurements on the cylinder surface.

The present paper deals with the ability of different numerical models to determine the heat transfer, under moderate Reynolds number conditions. We therefore more basically compare, for a selected moderate Reynolds number, the values of convective thermal power Φ_{conv} and temperature difference $(T_{surf} - T_i)$ obtained from different numerical simulations out of the experimental findings.

3. Numerical strategy

Numerical simulation might consist of two parts, which can be *modelling* and *numeric*. Any programmer or software user working in computational fluid dynamics needs to fully understand the physical reality of the case under study. Good knowledge of the case leads to the partial difference equations (PDE) to compute; this is the *modelling* part. The *numeric* part is concerned with the numerical method to solve by computation. Difficulties with computing arise mainly from the choice of the pair of methods (*modelling-numeric*). Generally, assumptions are made starting from the stronger to the lower ones until the computed result seems to be accurate or until the *modelling* is considered to be as close as possible to the physical reality of the case.

Since the air is moving at low speed (V=6.13 m/s, Mach=0.018) in such a complex geometry, hypotheses about fluid compressibility are relevant but not easy to define. Indeed, it is well known that the numerical resolution of the discrete form given by the PDE derived from the continuous model leads to significant problems when the Mach number approaches zero (M->0), especially regarding the degree of compressibility. On one hand the community working with incompressible flows would like to extend its application domains at least to weakly-compressible. Acoustic phenomena cannot be included in incompressible *modelling* because density is constant. On the other hand, the community working with compressible flows would like to predict low speed flows with accuracy. It is already known that the original set of the compressible PDE, with its numerical resolution methods which are supposed to give accurate solutions when flows are the seat of interface problems (like shocks, expansion waves or rarefactions), will provide a degeneration of the pressure field. This is the reason why two different modellings are investigated in this paper: incompressible *modelling* (IM) is studied using ANSYS-FLUENT and compressible *modelling* (CM) with ***elsA***. Both modellings have been worked on by several scientific communities since the beginning of the digital age. There are probably two main reasons: people from applied mathematics prefer working on IM while people in applied physics prefer CM.

ANSYS-FLUENT for incompressible modelling:

Historically the ANSYS-FLUENT software [1,2] has been used extensively in computational fluid dynamics (CFD) for a wide range of flow regimes (even compressible flows). In the *modelling* part, the original Navier-Stokes equations for compressible flows (i.e. PDE) have been modified in order to suppress acoustic phenomena. There are various possibilities, the most popular being density fixed as zero velocity divergence. Different combinations of PDE are possible in the *numeric* part. These apparent simplifications do not mean, however, that PDE is easy to solve from numerical standpoints.

The conservation laws (or PDE) of the fluid motion for laminar and steady state flows lead to the governing equations given below in Einstein notation.

Continuity:

$$\frac{\partial u_i}{\partial x_i} = 0$$

Momentum:

$$\rho u_j \frac{\partial u_i}{\partial x_j} = -\frac{\partial P}{\partial x_i} + \mu \frac{\partial^2 u_i}{\partial x_j^2}$$

Energy:

$$\rho u_j C_p \frac{\partial T}{\partial x_i} = \mu u_j \frac{\partial^2 u_i}{\partial x_j^2} - \frac{\partial q_i}{\partial x_i}$$

Where, u_i, ρ, T, P are the velocity components, density, temperature and pressure respectively. C_p, μ and k are the specific heat at constant pressure, the dynamic viscosity and thermal conductivity respectively. q_i is the local heat flux density given by Fourier's law: $q_i = -k \frac{\partial T}{\partial x_i}$. x_i and x_j are the directional components and t is time.

In this study the FLUENT CFX solver used for the incompressible flow application is the pressure-based one. Traditionally, the pressure updates are obtained via the resolution of an equation, which is a combination of two of the three (mass, momentum, energy) conservation equations. A Poisson equation is often employed, due to the fact that very efficient solvers already exist. Whatever the couple of mass/momentum equations chosen, segregated solvers are widely used in incompressible modelling. The energy equation is then solved alongside the others.

***elsA* for compressible modelling:**

The ***elsA*** software [3,4] is a multi-application CFD simulation platform dealing with internal and external aerodynamics from the low subsonic to the high supersonic flow regime. Concerning *modelling*, the set of PDE comes from the original conservative Navier-Stokes equations for compressible flow without any modification. Unlike with FLUENT, numerical resolution is made on the fully coupled system. Indeed, the compressible set of PDE solved in the present work is given below in Einstein notation.

Continuity:

$$\frac{\partial \rho}{\partial t} + \frac{\partial \rho u_i}{\partial x_i} = 0$$

Momentum:

$$\frac{\partial \rho u_i}{\partial t} + \frac{\partial}{\partial x_j} \rho u_i u_j = -\frac{\partial P}{\partial x_i} + \frac{\partial \tau_{ij}}{\partial x_j}$$

with the viscous stress tensor

$$\tau_{ij} = \mu \left(\frac{\partial u_i}{\partial x_j} + \frac{\partial u_j}{\partial x_i} \right) - \frac{2}{3} \mu \left(\frac{\partial u_k}{\partial x_k} \right) \delta_{ij}$$

Where δ_{ij} is the unit tensor (such that δ_{ij} is 1 if $i=j$ and 0 if $i \neq j$).

Energy:

$$\rho \frac{\partial}{\partial t} \left(C_v T + \frac{1}{2} \rho u^2 \right) + \rho u_j \frac{\partial}{\partial x_j} \left(C_v T + \frac{1}{2} u^2 \right) = -\frac{\partial}{\partial x_i} \left(p u_i \right) + \frac{\partial}{\partial x_j} \left(\tau_{ij} u_i \right) - \frac{\partial q_i}{\partial x_i}$$

Where u is the magnitude velocity.

This set of equations can be solved with different approximate Riemann solvers based on upwind or central schemes. The solvers of Roe [5] (upwind scheme) and Jameson [6] (central difference scheme) are chosen for this work.

The kind of numerical overview can be seen in Table 1 for both computer programs. In particular, they are both based on finite-volume methods under the laminar assumption. As a result, the spatial accuracy is at best of the second order. For the sake of code validation, two different solvers are tested for both modellings considered as incompressible-oriented and compressible-oriented respectively with FLUENT and ***elsA***.

Table 1. Numerical overview of FLUENT and ***elsA***

	FLUENT	***elsA***
Version	R15.0.7	V3.3-p2
Solver	Pressured-Based	Jameson and Roe
Time	Steady	Steady
Time marching	No	Implicit – irs
Models	Energy – ON Viscous – Laminar	Navier-Stokes laminar Viscosity Sutherland
Pressure-Velocity Coupling	Scheme – Simple or Piso	
Spatial Discretisation	Gradient – Least Squares Cell Based Pressure – Standard Density – Second Order Upwind Energy – Second Order Upwind	Second order central or upwind flux

4. Commented results

4.1. Presentation of the test case

Table 2 and Figure 4 summarize the physical boundary conditions for computation, which are given by the different measuring instruments (described in section 2) under standard laboratory conditions. In interpreting Table 2, it is important to remember that the two main choices are probably *steady* and *laminar*. The term *steady* means that the physical behaviour is related to an equilibrium problem. The term *laminar* means that no specific modelling is done to capture so-called turbulent eddies, with a wide range of length scales. The following results will emphasize the discussion about the choice of these physical assumptions.

Table 2. Physical boundary conditions.

Inlet and outlet	
Density	1.2 $kg.m^{-3}$
Pressure	101497.97 Pa
Inlet Temperature	294.65 K
Velocity magnitude	6.13 $m.s^{-1}$
Temperature - inner/heated wall	363.15 K
Temperature - external wall	333.25 K

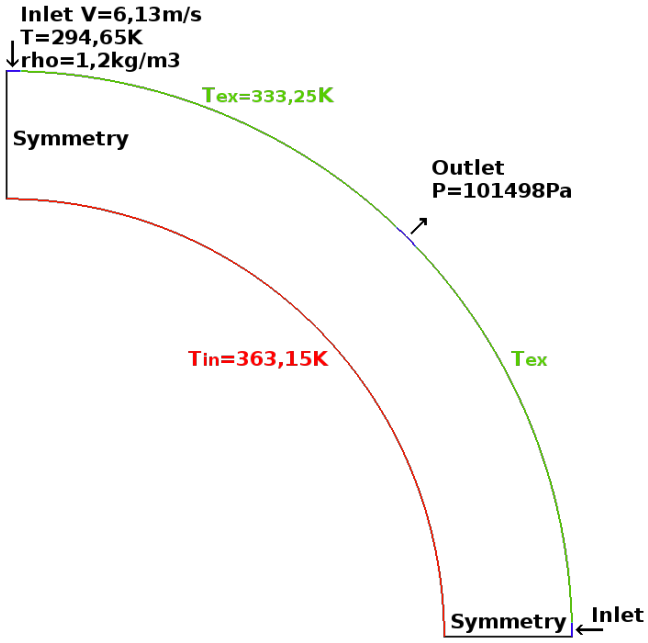

Fig. 4. Physical boundary conditions

More technical information on the selected options of each software can be found in Table 3.

*Table 3. Computing conditions with FLUENT and **elsA**.*

	FLUENT	***elsA***
Inlet	Massflow_inlet[1]	Injmfr1[2]
	Normal of inlets[3]=(0, -1, 0) or (-1, 0, 0)	Normal of inlets[3]=(0, -1, 0) or (-1, 0, 0)
	mass flux=7.36 $kg.m^{-2}.s^{-1}$	Surface mass flow=7.36 $kg.m^{-2}.s^{-1}$
	pressure = 101497.97 Pa	Stagnation enthalpy=296054.53 $m^2.s^{-2}$
	temperature = 294.65 K	
Outlet	Pressure_outlet[1]	Outpres[2]
	pressure = 101497.97 Pa	pressure = 101497.97 Pa
	temperature = 294.65 K	
Internal wall	wall[1]	wallisoth[2]
(heated wall)	temperature = 363.15 K	temperature = 363.15 K
External wall	wall[1]	wallisoth[2]
	temperature = 333.25 K	temperature = 333.25 K

In view of the geometry of the test case, we decided to make 2D computations only on one quarter of the full cavity seen in Figure 1. Also, axial symmetric conditions are supposed where x=0 and y=0. y=0 and x=0 are the basic horizontal and vertical axes, respectively. This geometric choice is motivated by computational timesaving but will lead to some disadvantages as mentioned below.

Grid independence study and code validations

For the numerical studies, a grid independency analysis was performed in order to select the optimal grid scale to optimize the computational time. For reasons of convenience and to save time, we decided to build the domain without the slots. To discretize the computational domain, a selection

[1] See Fluent user's guide
[2] See the User's reference manual of ***elsA***
[3] In the flow direction

of seven structured grids of different sizes (see Table 4, grids G0 to G6) were built and tested with the two numerical modellings for the four solvers. An approximate factor of 64 separates the coarser grid G0 with 3380 cells from the finer grid G6 with 212160 cells. Figure 5 shows the resulting wall heat flux. Starting from grid G3 the error rate on the average wall heat flux is lower than 2% for all computations and the local error of the radial wall heat flux does not reach 4%.

*Table 4. Selected grids for FLUENT and **elsA**.*

	G0	G1	G2	G3	G4	G5	G6
Number of nodes	3 654	7 047	13 572	26 883	53 505	106 743	213 237
Number of cells	3 380	6 760	13 260	26 520	53 040	106 080	212 160

The solutions are considered to be converged when the residuals decrease by five orders of magnitude for continuity, velocity components and energy. This is the case with FLUENT computations for both solvers SIMPLE and PISO. After this decrease, the residuals stabilize around a constant value, regardless of the computational time.

Using grid G3, residual behaviours with ***elsA***-Roe or ***elsA***-Jameson are the same, as shown in Figure 6. Though the steady case is observed after about 100,000 time iterations, the residual on the density, like any other physical conservative variables, is still decreasing and loses more than ten orders of magnitude on both calculations with Jameson and Roe. Moreover, the solutions are stable.

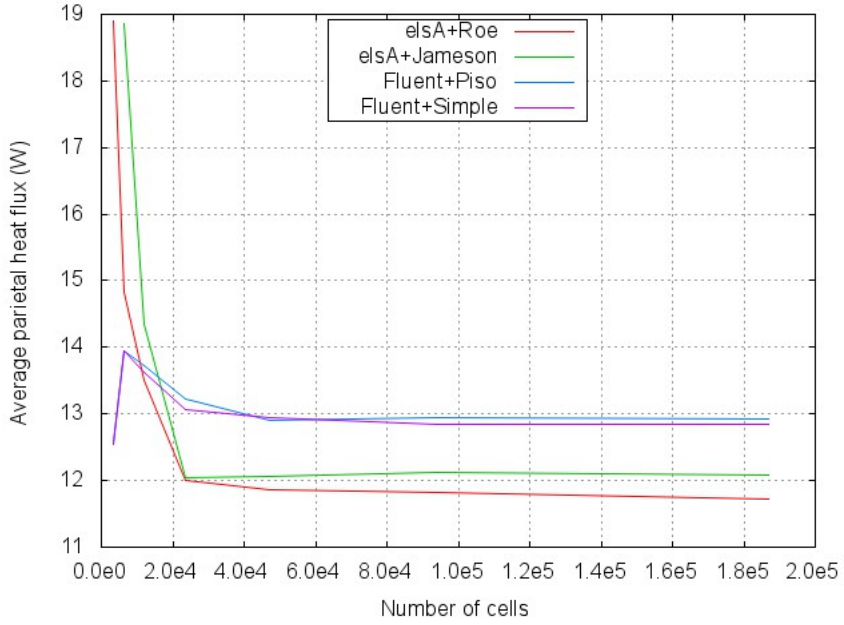

Fig. 5. Parietal heat flux for various grid densities.

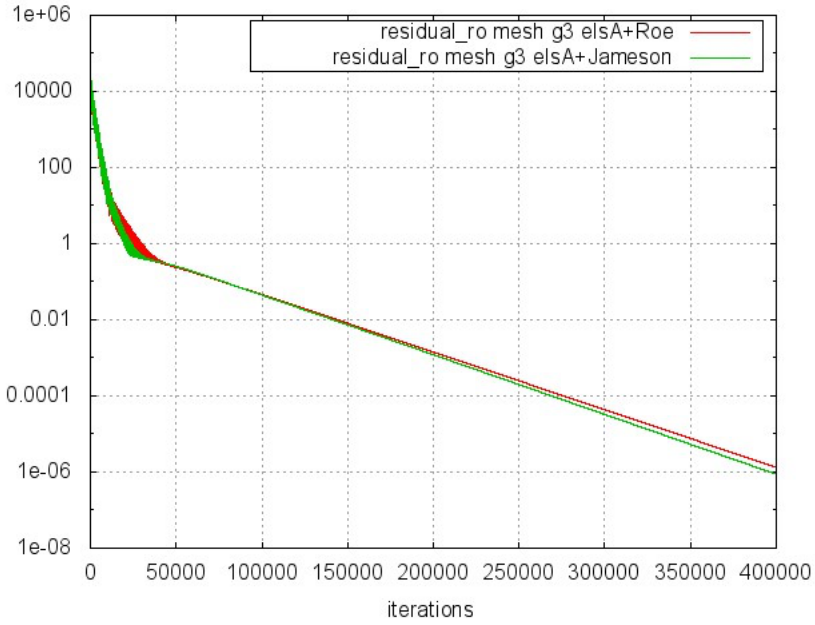

Fig. 6: Convergence history on the density (Rho) by elsA (Grid G3).

As indicated above, grid G3 was selected for all the following simulations. Details of this grid, shown in Figures 7a and 7b, are given in Table 5. Concerning lines 4 and 5 of Table 5, note that the parietal grid repartition is geometric.

*Table 5. Grid breakdown for FLUENT and **elsA**.*

	FLUENT /***elsA***
Number of points	26 683
Number of cells	26 520
Cell type	Quadrangular
Min and max edge size on the inner-heated cylinder (m)	$3.1e^{-5}$ to $0.5e^{-3}$
Min and max edge size on the outer cylinder (m)	$4.e^{-5}$ to $0.7e^{-3}$

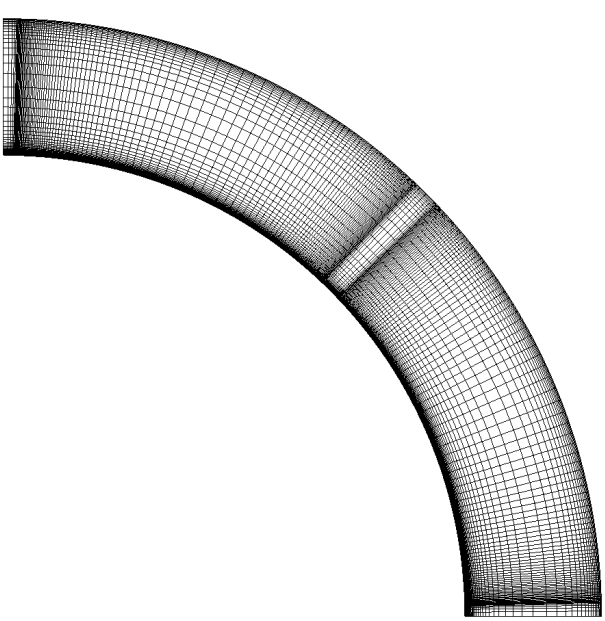

Fig. 7a Grid of the computational domain

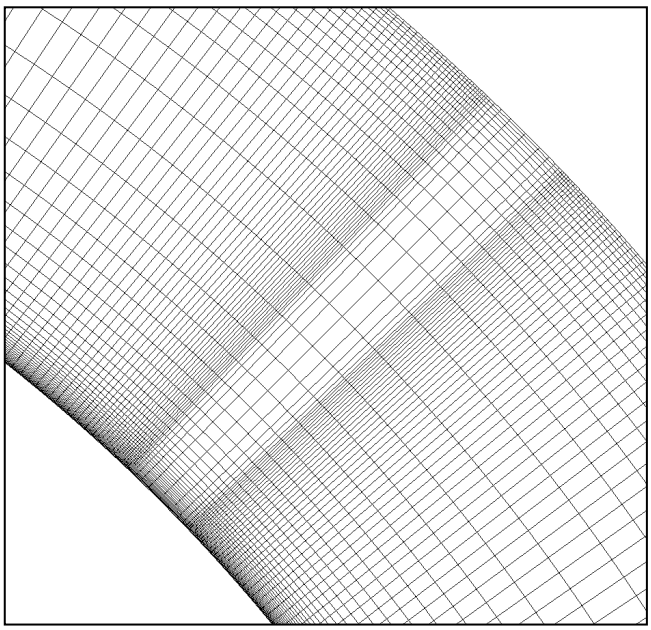

Fig. 7b Central zoom on the grid's cavity

4.2. ANSYS-FLUENT computations

In a very first step based on the incompressible flows assumption, two computational simulations are made with two discretisation schemes, which are SIMPLE [7] and PISO [8]. These numerical algorithms belong to the pressure-based family.

In both computations usual convergence criteria available in FLUENT are satisfied after 300,000 iterations. A transitional phase is observed for the first 20,000 iterations. Though the residuals fail for more than five orders of magnitude, a very slow flow regime which is more or less stable takes place in the central part of the cavity outside the viscous boundary layers. These low energy-consuming instabilities can be seen in Figures 8a and 8b where the eddy patterns are represented by streamlines. Nevertheless, when compared to SIMPLE, the solution obtained with the PISO algorithm is more stable. In Figures 8 the two colliding jets form a backflow fountain with two main vortices induced underneath the fountain (see Figure 8a). Two other, much smaller vortices stay at the inner-wall in the separation region.

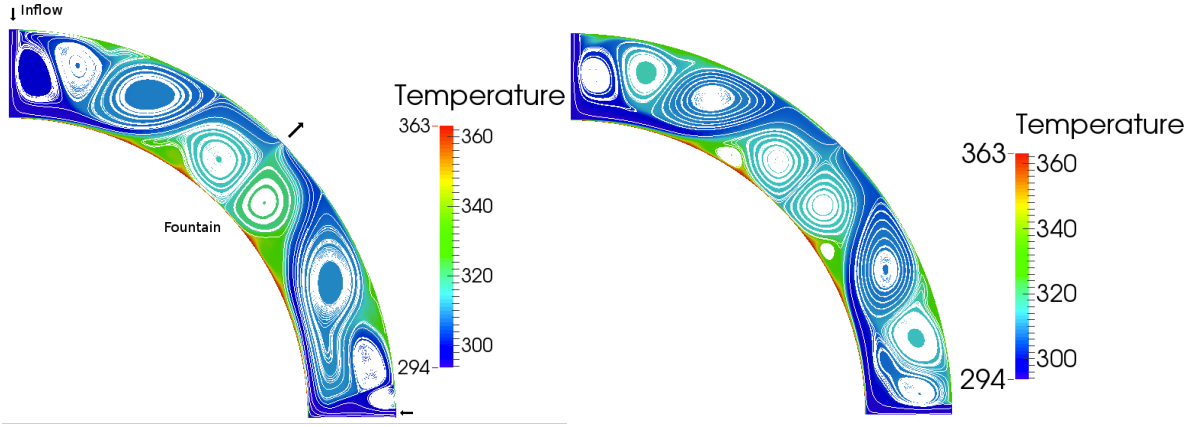

Fig. 8a. Left: Streamlines and temperature in a quarter domain by FLUENT+SIMPLE.

Fig. 8b. Right: Streamlines and temperature in a quarter domain by FLUENT+PISO.

Figure 9 (and Figure 12) represents the evolution of the conductive heat flux along the inner wall and coming from it. This flux is the consequence of the 250W electrical resistance inserted on the inner surface of the cylinder (see Figure 3a). Because of power leaks, the conductive heat flux is deduced from a wall temperature obtained by an average out of the 10 parietal thermocouples (see Section 2).

Despite the complexity and motion of the eddy patterns, the conductive heat flux evolution remains the same, as seen in Figure 9. It thus appears that the amount of energy absorbed by the moving eddies is relatively weak. Though the residuals fail for more than five orders of magnitude, a very slow flow regime which is more or less stable takes place in the central part of the cavity outside the viscous boundary layers. These low energy-consuming instabilities can be seen in Figures 8a and 8b where the eddy patterns are represented by streamlines. Nevertheless, when compared to SIMPLE, the solution obtained with the PISO algorithm is more stable. In Figures 8 the two colliding jets form a backflow fountain with two main vortices induced underneath the fountain (see Figure 8a). Two other, much smaller vortices stay at the inner-wall in the separation region.

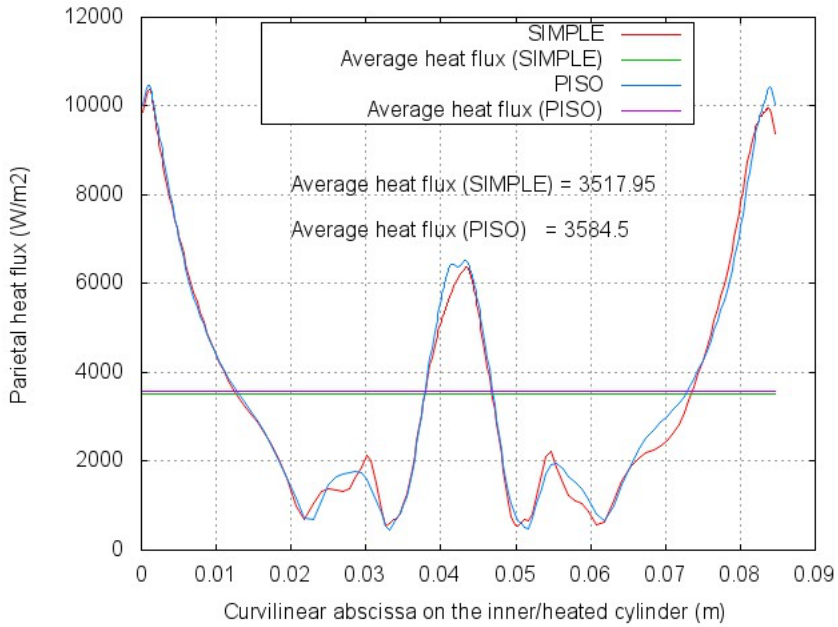

Fig. 9. Parietal evolution of the conductive heat flux of the inner-heated cylinder by FLUENT.

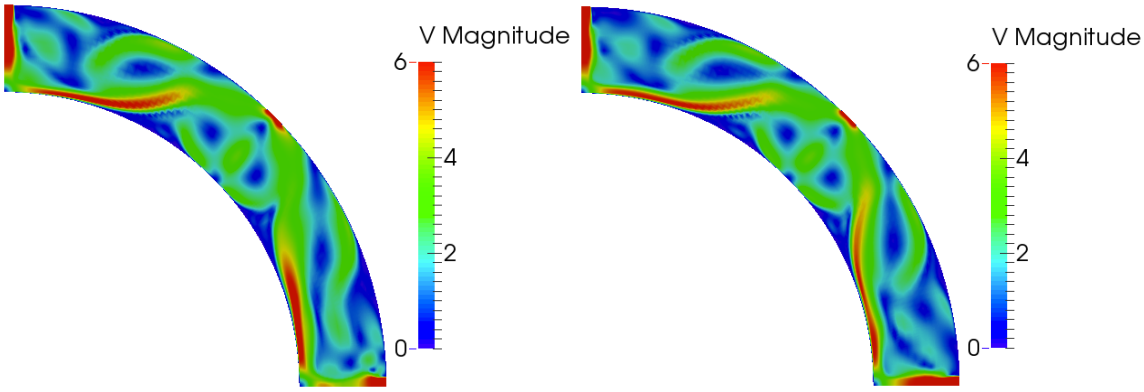

Fig. 10a. Left: Velocity in a quarter domain by FLUENT+SIMPLE.

Fig. 10b. Right: Velocity in a quarter domain by FLUENT+PISO.

Figures 10 show views of the velocity magnitude contours of the computational domain for both incompressible solvers. Though these patterns are slightly different, the flow field properties observed are the same. As already seen in Figures 8-9, the velocity fields show three distinct freejets, stagnation, wall-jet and fountain regions. The wall-jet region extended for about one-height of the circumference beyond the stagnation region before it detached. In this region the velocity magnitude of the flow reaches its maximum forming the main streamlines, which are flowing toward the exit. The detachment jet clearly visible in Figures 10, which correspond to the first separation point, is halfway between the stagnation point and the fountain.

4.3. *elsA* computations

In a second step, based on the compressible flows assumption, two computational simulations are made with two different approximate Riemann solvers, which are commonly known as Jameson and Roe. The two main numerical methods to solve the compressible model are based on either central schemes or upwind schemes. Jameson and Roe solvers are respectively chosen to represent both methods.

Figures 11a and 11b confirm previous findings about stability. The eddy patterns are reduced to six distinctive vortices in a perfect symmetry.

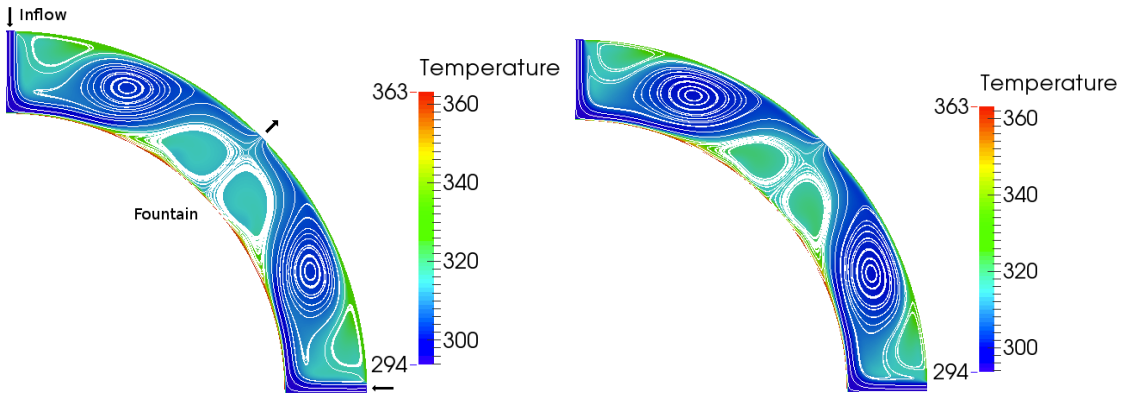

*Fig. 11a. Left: Streamline and temperature inside the cavity by **elsA**+Jameson.*

*Fig. 11b. Right: Streamline and temperature inside the cavity by **elsA**+Roe.*

In Figure 12, the heat flux behaviours of both solutions are mainly the same except at the air jets' stagnation point (x=0m and x=0.084m) and at the fountain (x= 0.042m). Averages on both fluxes are equivalent, at less than 4.5% in relative value. The minima of the parietal wall heat flux occurred at and just downstream of the separation point. The transfer properties downstream of the separation point were governed by the transport under a strong recirculating fountain. The parietal heat flux distributions for the cylinder are similar to those seen in Figure 9, except in two respects. First, there is only one separation point in Figure 12 whereas there are two in Figure 9. Second, the magnitude of the peak centred under the fountain is about half as high in Figure 12 as that seen in figure 9.

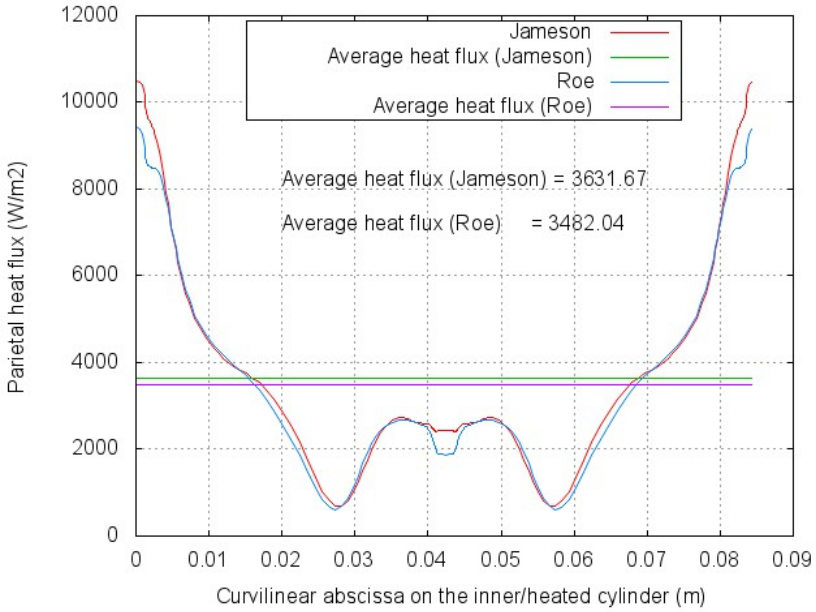

*Fig. 12. Parietal inner conductive heat flux evolutions by **elsA**.*

Examination of the velocity field for the jet on the cylindrical target in Figures 13 have some similarities with those seen in Figures 10. The zones of maximum velocities are at the same locations along the inner-wall and form a stream-tube flowing toward the exit before rounding the

vortices underneath the fountain. As also shown in Figure 12, the single separation point is located in the precise middle of the two separation points seen in Figure 9 (see also Figure 14).

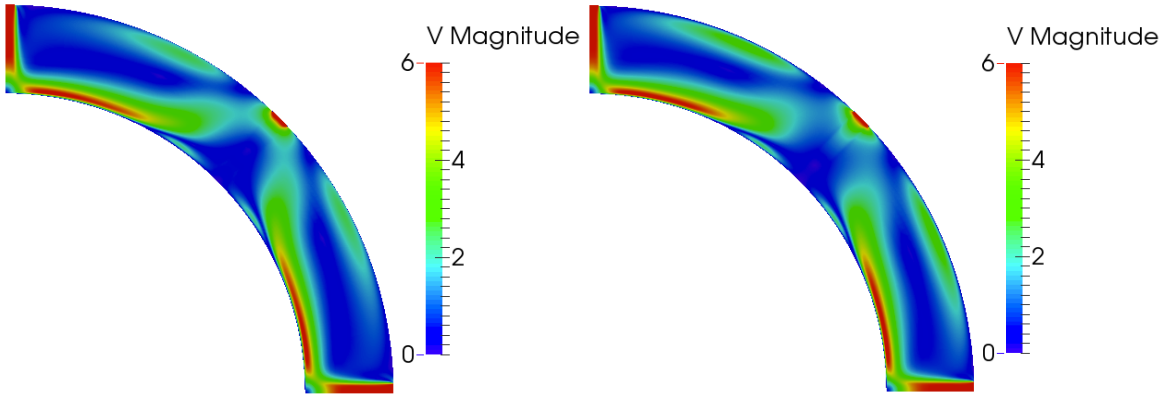

*Fig. 13a. Left: Velocity inside the cavity by **elsA**+Jameson.*

*Fig. 13b. Right: Velocity inside the cavity by **elsA**+Roe*

4.4. Comparisons between FLUENT-*elsA* and Numerical-Experiment

Table 6 shows the percentages of error in mass flow rates for the 4 computations. Though the exact inlet value of the mass flow rate is known, an error rate ranging from -0.008% to -0.01% is noted for the set of computations. This relatively small error mainly comes from the way that both codes calculate the inlet mass flow rate from the inlet read boundary conditions, which are mass flow and stagnation enthalpy for elsA and mass flow, pressure and temperature for FLUENT. The last two lines of Table 6 show the outlet mass flow rate in each computational case and the error over inlet. With FLUENT, errors range from -0.30% to 0.49% with PISO and SIMPLE. The less-volatile PISO solutions give slightly better estimations of the exit mass flow rates than the solutions using SIMPLE. With ***elsA***, errors are of two orders of magnitude lower as those obtained using FLUENT and more stable than both FLUENT solvers.

*Table 6. Error on the inlet/outlet mass flow rate with FLUENT and **elsA**.*

	Experiment	*FLUENT with SIMPLE*	*FLUENT with PISO*	***elsA*** with Jameson	***elsA*** with Roe
Inlet mass flow rate ($kg.s^{-1}$)	0.001245	0.0012448	0.0012449	0.0012448	0.0012448
Error rate (over the experiment)		-0.01%	-0.008%	-0.01%	-0.01%
Outlet mass flow rate ($kg.s^{-1}$)	0.001245	0.001241 to 0.001251	0.001243 to 0.001250	0.0012447	0.0012447
Error rate of the outlet mass flow over inlet		-0.30% to 0.49%	-0.15% to 0.41%	-0.008%	-0.008%

In Table 7, convective heat fluxes ($\Phi_{conv} = \dot{m} c_p (T_e - T_i)$) are given, with FLUENT and ***elsA*** respectively. Both tables also give the comparison between computations and the experiment. The difference in convected heat fluxes between the computations (from 17.97W to 24.17W with SIMPLE and 25.74W with Jameson) and the experiment (27W) mainly comes from the heat exchanges occurring in the third dimension through the sidewalls. Indeed, there is no thermal insulation between the heated cylinder and the sidewalls. As a consequence, the additional power from the sidewalls, which is naturally included in the experimental measurement, cannot be taken

into account in the 2D computation. This point may explain why the convected heat fluxes from the 2D computation are always lower than those from the experiment. Despite the fact that the SIMPLE algorithm is more unstable than PISO's, error rates are very much the same, ranging from -35% to -13%.

*Table 7. Convected heat flux comparisons with FLUENT and **elsA**. Experiment is the reference.*

	Experiment	*FLUENT with SIMPLE*	*FLUENT with PISO*	***elsA*** with Jameson	***elsA*** with Roe
Convected heat flux (W)	27.65	17.97 to 24.17	18.08 to 21.38	25.74	22.56
Error rate over the experiment		-35% to -13%	-35% to -23%	-7%	-18%
Ratio over the experiment		0.65 to 0.87	0.65 to 0.77	0.93	0.82

Though the ***elsA*** solutions are stable, the difference between the error rates is relatively high between the two solvers (Jameson and Roe). Compared to the experiment, the error rate is -18% with Roe and -7% with Jameson. This difference may come from the nature of the numerical scheme and its associated dissipation. It is well known that central differencing (like Jameson) provides no mechanism for dissipation. Central differencing methods require the addition of some form of artificial dissipation, which can be reduced to nothing when the flow is not the seat of nonlinear effects, such as shocks. On the other hand upwind schemes (like Roe) have an inherent amount of internal dissipation, due to the one-sided differences, which is usually difficult to modify or decrease. It can be shown that upwind schemes have an equivalence to central difference schemes with added dissipation.

Figure 14 depicts the final comparison between the inner-heat-wall flux evolution FLUENT-PISO and ***elsA***-Jameson. The behaviour of these curves seems to be a consequence of the swirling structure (already seen in Figures 7 and 12). Positions x=0 and x=0.084 correspond to the axes of two impacting jets and their respective heat fluxes are maximal, as expected. Starting from these extremities, both fluxes globally decrease along the cylinder before increasing near the outlet slot axis. Though the curve profiles are not strictly identical, the fluxes' average values are the same within 1.3%.

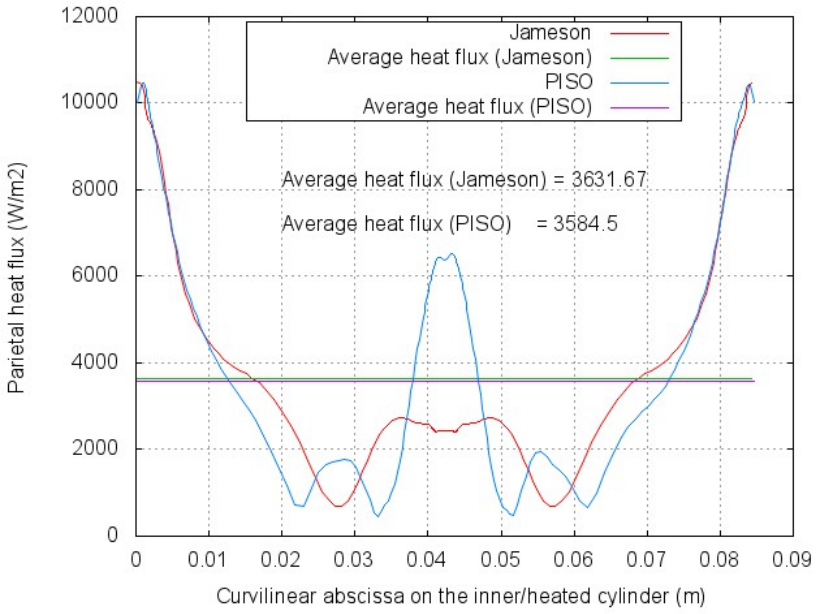

*Fig. 14. Parietal inner conductive heat flux comparison between **elsA** and FLUENT.*

5. Conclusion and perspectives

In the context of green aircraft projects, the trend toward increasing use of electrical engines requires more and more efficient cooling systems. In this study, a specific cooling system based on four air jets impacting on a heater cylinder has been tested. This laboratory facility, located at Pau University (France), is devoted to the study of small-sized turbo engines.

In parallel, numerical simulations of convective heat transfer were conducted. Simulating the laboratory test case allowed a comparison with experimental data, but an additional goal was to achieve a comparison between numerical codes by solving the Navier-Stokes equations for incompressible or compressible fluids. This comparison was made by using FLUENT's incompressible model and ***elsA***'s compressible code under the assumption of laminar flows.

Two different solvers for both fluid assumptions where tested in the interest of code validation. The flow fields obtained by the two codes show that eddy patterns in the simulated annular domain compared well on a coarse scale. The main stream-tubes from inlet to outlet have similar shapes. Diameters of the large-scale eddies in the recirculating fountain are approximately the same for both models. Though convergence rates are relatively low with FLUENT's incompressible code, the two different numerical methods employed display unsteadiness even under steady boundary conditions. As a consequence, the expected symmetrical nature of the flow field is dropped when the fluid is supposed to be incompressible. In contrast to previous incompressible findings, compressible CFDs give more stable results, which preserve the symmetry of the flow in accordance with the geometry of the cavity.

On a smaller scale, despite the notable differences stated previously between incompressible and compressible, the averages of some physical values are in good agreement. Indeed, the parietal inner conductive heat fluxes differ along the wall while their average values are the same within 1.3%.

The total convective heat transfer predicted by numerical simulations is in rough agreement with the results of the laboratory experiment for the FLUENT incompressible code ranging from 0.65 to 0.87 of the laboratory value, as compared to the results of the compressible ***elsA*** code ranging from 0.82 to 0.93 of the experimental value. Compressible effect considerations, even at a low Mach number, give the best agreement between the numerical simulation and the experiment. In addition, the conservation of mass flow rates between inlet and outlet is better achieved by ***elsA***'s compressible code than by FLUENT's incompressible code.

However, here it is far too early to draw any qualitative conclusion about the resulting findings in both models and further improvements are required.

It is encouraging that the results of simulations are in qualitative agreement with the laboratory experiments and that they recover the magnitude order of the total heat transfer measured. Nevertheless, much remains to be done including 3D computations, among others. Modelling compressible fluid flows in low Mach number conditions is known to be quite a difficult task. Our goal is to move towards the development of “All Mach” solvers.

Acknowledgments

First of all the authors would like to thank Pau University (UPPA-France), the Conseil Régional d'Aquitaine and SAFRAN-Turbomeca for their financial support for the PhD thesis of Nicolas CHAUCHAT. Secondly, special thanks to ONERA for their invaluable day-to-day help in the best possible use of the ***elsA*** software. Finally, as mentioned above, in the case of the selected research program by the three French aeronautical competitiveness clusters (Aerospace Valley, ASTech and PEGASE), part of this research was supported by public funding from the DGE (Direction Générale des Entreprises).

References

[1] Franklyn J. Kelecy. Coupling momentum and continuity increases CFD robustness, ANSYS advantage, volume II, issue 2, 2008.

[2] ANSYS Fluent software contains the broad physical modelling capabilities needed to model flow, turbulence, heat transfer, and reactions for industrial applications. Available at: <http://www.ansys.com/Products/Simulation+Technology/Fluid+Dynamics/Fluid+Dynamics+Products/ANSYS+Fluent> [accessed 21.1.2015].

[3] Laurent Cambier, Sébastien Heib, and Sylvie Plot. The ONERA ***elsA*** CFD software : input from research and feedback from industry. Mechanics & Industry, 14(03) :159–174, 2013.

[4] ***elsA*** is the ONERA software for complex external and internal flow simulations and for multi-disciplonary application involing aerodynamics. Available at: <http://elsa.onera.fr> [accessed 21.1.2015].

[5] P. L. Roe. Approximate Riemann Solvers, Parameter Vectors, and Difference Schemes. J. Comput. Phys., 43:357–372, 1981.

[6] A. Jameson, W. Schmidt, and E. Turkel. Numerical Solution of the Euler Equations by Finite Volume Methods using Runge–Kutta Stepping Schemes. Technical Report 81–1259, AIAA, 1981.

[7] S.V. Patankar and D.B. Spalding, "A calculation procedure for heat, mass and momentum transfer in three-dimensional parabolic flows", International Journal of Heat and Mass Transfer, Vol. 15, pp. 1787-1806 (1971).

[8] Issa, R. I. (1986). Solution of the implicitly discretised fluid flow equations by operator-splitting, J. Comput. Phys., Vol. 62, pp. 40-65.

[9] R. Gardon, J.C. Akfirat, The role of turbulence in determining the heat-transfer characteristics of impinging jets, Int. J. Heat Mass Transfer 8 (1965) 1261-1272.

[10] H. Martin, Heat and mass transfer between impinging gas jets and solid surfaces, Adv. Heat Transfer 13 (1977) 1-60.

[11] K. Jambunathan, E. Lai, M.A. Moss, B.L. Button, A review of heat transfer data for single circular jet impingement, Int. J. Heat Fluid Flow 13 (1992) 106-115.

[12] Gardon R, Akfirat J. 1966. Heat transfer characteristics of impinging two-dimensional air jets. J Heat Transf 88:101–8.

[13] N. Zuckerman, N. Lior, Jet impingement heat transfer: physics, correlations, and numerical modeling, Adv. Heat Transf. 39 (2006) pp.565-631.

[14] N. Zuckerman, N. Lior, Radial slot jet impingement flow and heat transfer on a cylindrical target, Journal of Thermophysics and Heat Transfer 21 (3) (2007) 548–561.

[15] D. Singh, B. Premachandran, Sangeeta Kohli, Experimental and numerical investigation of jet impingement cooling of a circular cylinder, International Journal of Heat and Mass Transfer 60 (2013) 672–688.

[16] D. Singh, B. Premachandran, S. Kohli, Circular air jet impingement cooling of a circular cylinder with flow confinement, International Journal of Heat and Mass Transfer 91 (2015) 969–989.

[17] D. Singh, B. Premachandran, S. Kohli, Effect of nozzle shape on jet impingement heat transfer from a circular cylinder, International Journal of Thermal Sciences 96 (2015) 45-69.

[18] X.L. Wang a, D. Motala b, T.J. Lu a, S.J. Song c, T. Kim b, Heat transfer of a circular impinging jet on a circular cylinder in crossflow, International Journal of Thermal Sciences 78 (2014) 1-8.

[19] F. Gori, L. Bossi, On the cooling effect of an air jet along the surface of a cylinder, International Communications in Heat and Mass Transfer 27 (2000) 667–676.

[20] C.S. McDaniel, B.W. Webb, Slot jet impingement heat transfer from circular cylinders, International Journal of Heat and Mass Transfer 43 (2000) 1975-1985.

[21] D. H. Lee a, J. R. Bae, H. J. Park, J. S. Lee, P. Ligrani, Confined, milliscale unsteady laminar impinging slot jets and surface Nusselt numbers, International Journal of Heat and Mass Transfer 54 (2011) 2408–2418.

[22] H. Shariatmadar, A. Momeni, A. Karimi, M. Ashjaee, Heat transfer characteristics of laminar slot jet arrays impinging on a constant target surface temperature, Applied Thermal Engineering 76 (2015) 252-260.

[23] V.N. Korovkin, Yu.A. Sokovishin, Variation of heat transfer in laminar wall jets with different initial velocity profiles, Appl. Therm. Sci. 2 (1989) 30–32.

[24] Gardon R, Akfirat J. 1966. Heat transfer characteristics of impinging two-dimensional air jets. J. Heat Transf. 88:101–8.